Journal of the Taiwan Institute of Chemical Engineers 143 (2023) 104675

Contents lists available at ScienceDirect

Journal of the Taiwan Institute of Chemical Engineers

journal homepage: www.journals.elsevier.com/journal-of-the-taiwan-institute-of-chemical-engineers

Materials Science and Technology

Functional role of B-site substitution on the reactivity of $CaMFeO_3$ (M = Cu, Mo, Co) perovskite catalysts in heterogeneous Fenton-like degradation of organic pollutant

Rasyidah Alrozi [a,b], Nor Aida Zubir [a,b,c,*], Noor Fitrah Abu Bakar [d], Bradley P. Ladewig [e], Julius Motuzas [f], Noor Hana Hanif Abu Bakar [g], David K. Wang [h], João C. Diniz da Costa [f,i,j]

[a] Centre for Chemical Engineering Studies, Universiti Teknologi MARA, Cawangan Pulau Pinang, 13500 Permatang Pauh, Pulau Pinang, Malaysia
[b] Hybrid Nanomaterials, Interfaces & Simulation (HYMFAST), Centre for Chemical Engineering Studies, Universiti Teknologi MARA, Cawangan Pulau Pinang, 13500 Permatang Pauh, Pulau Pinang, Malaysia
[c] Water Research and Environmental Sustainability Growth (WAREG), Universiti Malaysia Perlis (UniMAP), 02600 Arau, Perlis, Malaysia
[d] School of Chemical Engineering, College of Engineering, Universiti Teknologi MARA Shah Alam, 40450 Shah Alam, Selangor, Malaysia
[e] Karlsruhe Institute of Technology, Institute for Micro Process Engineering, 76344 Eggenstein-Leopoldshafen, Germany
[f] The University of Queensland, FIM^{2}Lab—Functional Interfacial Materials and Membranes Laboratory, School of Chemical Engineering, Brisbane, Qld 4072, Australia
[g] Nanoscience Research Laboratory, School of Chemical Sciences, Universiti Sains Malaysia, 11800 Penang, Malaysia
[h] School of Chemical and Biomolecular Engineering, The University of Sydney, New South Wales 2006, Australia
[i] LAQV-REQUIMTE, (Bio)Chemical Process Engineering, Department of Chemistry, Faculty of Science and Technology, Universidade NOVA de Lisboa, 2829-516 Caparica, Portugal
[j] iBET – Instituto de Biologia Experimental e Tecnológica, 2781-901 Oeiras, Portugal

ARTICLE INFO

Keywords:
Perovskites
B-site substitution
Reactivity
Fenton-like
Degradation
Organic pollutant

ABSTRACT

Background: Substitution of different types of B-site metal cations in the perovskite structure led to a significant change in the catalytic reactivity of the resulting catalysts. In this work, the functional role of B-site substitution on the catalytic reactivity of mixed oxides containing B-site substituted $CaMFeO_3$ (M = Cu, Mo and Co) perovskite catalysts is investigated.

Methods: The catalysts were synthesized via a modified EDTA-citric acid complexation method and tested for the heterogeneous Fenton-like reaction for oxidative degradation of acid orange II (AOII) dye in the presence of H_2O_2.

Significant findings: $CaCuFeO_3$ exhibited the highest AOII degradation (97%) followed by $CaMoFeO_3$ (90%), $CaFeO_3$ (64%) and $CaCoFeO_3$ (40%) within 60 min of reaction, and the reaction followed a pseudo-second-order kinetics model. Interestingly, the partial substitution of Cu in the B-site of $CaFeO_3$ enhanced the reaction rate constant achieving a k value of 1.9×10^{-2} L mg^{-1} min^{-1}, approximately twenty-one times higher than that of the blank catalyst $CaFeO_3$. The enhanced catalytic reactivity of $CaCuFeO_3$ is associated with the high reducibility of copper/iron ions within the B-site structure in the presence of oxidant which facilitated fast redox cycling of the active sites during catalysis. The fast redox cycling is attributed to the decent electron mobility due to low electron transfer resistance between the active sites.

1. Introduction

Synthetic dyes are a prominent source of industrial pollution and water contamination [1,2]. The residual dyes are not readily biodegradable and can be found in wastewater effluents originated from textile, paper, leather, cosmetics and other industries. The most common type of synthetic dye used in the textile industry is azo dyes, accounting for half of all the commercial dyes [3]. These dyes are characterized by the existence of one or more azo (-N = N-) bonds. Despite its versatile use and chemical stability, azo dyes have been reported to be carcinogenic and mutagenic contaminants with poor environmental biodegradability [4]. In fact, the dissolution of azo dyes in water can caused discoloration

* Corresponding author at: School of Chemical Engineering, College of Engineering, Universiti Teknologi MARA, Cawangan Pulau Pinang, Permatang Pauh, Pulau Pinang 13500, Malaysia.
E-mail address: noraida709@uitm.edu.my (N.A. Zubir).

https://doi.org/10.1016/j.jtice.2023.104675
Received 21 September 2022; Received in revised form 31 December 2022; Accepted 5 January 2023
Available online 15 January 2023
1876-1070/© 2023 Taiwan Institute of Chemical Engineers. Published by Elsevier B.V. All rights reserved.

of the surface water, which hinders light penetration. As a result, the photosynthesis activities of marine flora will be affected and thus negatively impacting the aquatic marine organism's food source. Hence, untreated dyes pose a significant threat to human health and marine ecosystems. Various physical, biological and chemical treatment methods [5,6] have been developed and applied to overcome this issue. The physical treatments such as adsorption, membrane filtration and coagulation-flocculation typically require additional treatment as they are seriously affected by secondary pollution whilst the complete degradation of dye pollutant remain unsolved [7]. On the other hand, biological treatments have several drawbacks, including the need for longer retention time [8], and wastewater treatment plants with large footprint.

Advanced oxidation processes (AOPs) have been broadly used as water/wastewater treatment methods due to the generation of hydroxyl radicals ($^{\bullet}OH$), which can rapidly and non-selectively degrade a wide range of organic pollutants. Fenton's reagent [9,10] and ultra-violet/hydrogen peroxide (UV/H_2O_2) [11,12] are the most common type of AOPs. In principle, the $^{\bullet}OH$ is generated when H_2O_2 is activated by iron ions or UV during catalysis. For instance, the Fe^{2+}/H_2O_2 process degraded >98% of AO7 dye solution within 1 h [13], while UV/H_2O_2 exhibited complete degradation of AO7 after 30 min of reaction [14]. However, homogeneous oxidation processes have several disadvantages, including a narrow pH range of catalytic oxidation, catalyst deactivation, the need for catalyst regeneration, and the removal of iron compounds from the treated water [15]. Moreover, irradiation of UV light during reaction requires high energy consumption [16,17] and photocatalytic reactivity depends on UV light source availability and intensity [18]. Hence, there is a great benefit to develop heterogeneous catalysts that can initiate oxidation reactions without the need for illumination.

Modification of compounds containing iron oxides have been studied for the degradation of dyes, using graphene oxide [19,20], metal-organic frameworks (MOF) [21,22] and mixed oxides such as perovskites [23–25], whereas the latter is generally considered desirable for heterogeneous catalytic applications. Perovskites are crystalline ceramics that belong to the class of mixed oxides with a general formula of ABO_3. A-site cation is commonly occupied by alkali metals, alkaline-earth metals or rare-earth metals. The B-site cation could be filled by transition metals. Perovskite can be formulated into binary (ABO), ternary (AA'BO or ABB'O) or quaternary (AA'BB'O) compounds. Interestingly, the perovskite's catalytic reactivity can be modulated by substituting different A and/or B cation types within the structure to control the overall physicochemical properties of the perovskites. In addition, it was reported that the catalytic reactivity of the perovskite is affected by the partial substitution of the B-site with different transition metal cations [26]. For instance, the partially substituted Cu in $LaCoO_3$ in the B-site formed a tertiary $LaCoCuO_3$ perovskite for the degradation of phenol that boosted the catalytic performance of by approximately 99% within 12 min [27]. Quaternary perovskites also proved to be efficient heterogeneous catalyst for organic dye degradation. For example, $Ca_{0.5}Sr_{0.5}Ni_xCu_{1-x}O_{3-\delta}$ degraded 95% of AOII within 2 h, which was attributed to the effective redox cycles between $\equiv Ni^{2+}/\equiv Cu^{1+}$ and $\equiv Ni^{3+}/\equiv Cu^{2+}$ for the generation of reactive radical species during catalysis [28]. The synergistic interaction between Ni and Fe was also positive for $CaNi_xFe_{1-x}O_{3-\delta}$ perovskites showing over 50% degradation of Reactive Red 141 and AOII after 5 min reaction time [29].

In the case of B-site perovskite catalyst containing Cu/Fe and Co/Fe, the typical type of A-site substitutions are based mainly on La [30,31], Bi [32], Sr [33,34] and Ba/Sr [35]. A number of mixed oxides containing Ca in the A-site perovskites such as $Ca_xSr_{1-x}CuO_{3-\delta}$ [36], $Ca_{0.5}Sr_{0.5}Ni_xCu_{1-x}O_{3-\delta}$ [28], $CaNi_xFe_{1-x}O_{3-\delta}$ [29] and $Ca_{0.5}Sr_{0.5}NiO$ [37] were also effective in the degradation of AOII dyes. Ca is particularly effective in the A-site of some of these catalysts, but limited work has been reported for compounds containing Fe oxides in the B-site. Herein, we investigate the functional role of B-site substitution on the calcium-iron-based mixed oxide perovskite catalysts; $CaMFeO_3$ (M = Mo, Cu, Co) for H_2O_2 activation in heterogeneous Fenton-like reaction. AOII was chosen as model pollutants as it represents 15% of worldwide dye production [38] and the most discharged dye from the textile industry [36,39]. In this study, $CaMFeO_3$ (M = Mo, Cu, Co) mixed oxides containing perovskite synthesized via EDTA citric acid complexation method were prepared and their catalytic activities were investigated in the absence and presence of H_2O_2. The functional role of transition metals on substituted $CaMFeO_3$ towards AOII degradation rate was evaluated using reaction kinetics models and mechanistic understanding was correlated to their resultant physicochemical properties.

2. Materials and methods

2.1. Synthesis and characterization

Calcium nitrate tetrahydrate ($Ca(NO_3)_2{\cdot}4H_2O$; ≥99%), iron(III) nitrate nonahydrate ($Fe(NO_3)_3{\cdot}9H_2O$; 99%), ammonium molybdate ($(NH_4)_2MoO_4$; 99%), cobalt(II) chloride hexahydrate ($CoCl_2{\cdot}6H_2O$; 98%), copper(II) nitrate trihydrate ($Cu(NO_3)_2{\cdot}3H_2O$; ≥99%), ethylenediaminetetraacetic acid (EDTA), ammonium hydroxide (NH_4OH) solution, hydrogen peroxide (H_2O_2; 30% (w/w)) and acid orange II (AOII) were supplied by Sigma Aldrich. Citric acid monohydrate ($C_6H_8O_7.H_2O$; ≥99%) was purchased from QReC (Asia). All chemicals were of analytical grade and used as received without further purification.

The EDTA-citric acid complexation method was used to synthesize a series of B-site-substituted $CaMFeO_3$ (M = Mo, Co, Cu) perovskites in this study. Each A/B-site cation molar concentration was fixed at 0.05 M A set of molar ratios of A-site precursor: B'-site precursor: B-site precursor: ethylenediamine tetra-acetic acid (EDTA): citric acid: ammonium hydroxide was kept constant at 1:1:1:1.1:2:10. For instance, in the synthesis of $CaMoFeO_3$ catalyst, 0.05 M $Ca(NO_3)_2{\cdot}4H_2O$, 0.05 M $FeCl_3{\cdot}6H_2O$, 0.05 M $(NH_4)_2MoO_4$ and 0.1 M $C_6H_8O_7.H_2O$ solutions was mixed and stirred for 15 min at the beginning. Then, a solution mixture containing 0.05 M NH_4OH and 0.055 M EDTA was added to the former mixture and stirred for 15 min at room temperature until well mixed.

Subsequently, the resultant homogeneous mixture was heated at 100°C under stirring to evaporate water to form a viscous solution. Further gelation of the viscous solution was carried out in the oven at 90°C for 24 h. The dried gel samples then underwent a two-stage sintering process in a muffle furnace: first stage at 450°C for 8 h and second stage at 800°C for 4 h at a ramping rate of 5°C min^{-1} in air. The resultant $CaMoFeO_3$ perovskite was ground and stored prior to further use. Similar procedures were repeated for other substituted B-site perovskite catalysts using copper and cobalt precursors to synthesize $CaCuFeO_3$ and $CaCoFeO_3$, respectively. In addition, $CaFeO_3$ was also synthesized as a blank catalyst for comparison purposes.

The phase identification of the materials was performed by X-ray powder diffraction (XRD, D8 Advance, Bruker, USA) with Cu-Kα radiation (λ = 1.5406 Å) at 40 kV and 40 mA by step scanning in the range of $10° \leq 2\theta \leq 100°$. The surface morphology was analyzed using a field emission scanning electron microscope (FE-SEM), equipped with energy-dispersive X-ray spectroscopy (EDS) for elemental analysis. Nitrogen adsorption analysis was carried out at 77 K using a Micromeritics ASAP 2020 to determine the BET surface area of samples that were degassed overnight at 200°C under vacuum.

Oxygen-temperature-programmed desorption (O_2-TPD) analysis was performed using AutoChem II 2920 (Micromeritics). Each sample (100 mg) was pretreated in helium (carrier gas, 50 mL min^{-1}) from room temperature to 350°C for 30 min at a rate of 10°C min^{-1}. After cooled down to 50°C, the sample was saturated by pure oxygen gas (50 mL min^{-1}) for 1 h then purged with helium (50 mL min^{-1}). After acquiring a stable baseline, the catalyst was heated to 800°C at 5°C min^{-1} ramping rate, and the O_2-TPD profile was recorded. For hydrogen-temperature-

programmed reduction (H_2-TPR), the analysis was conducted using the same instrument as in the O_2-TPD procedure. Initially, 100 mg of each sample was pretreated in helium to 350°C (at 10°C min^{-1}) for 1 h. After cooling to 50°C, the helium was switched to hydrogen flow (10 vol% H_2 in Ar, 50 mL min^{-1}). Once stable baseline acquired, the H_2-TPR profile of the catalyst was recorded while heating to 800°C at a rate of 5°C min^{-1}. Details analysis on the determination of pH zero-point charge (pH_{zpc}), ions metal leaching and the electrical impedance spectroscopy analysis are summarized in Supplementary Information (Text S1).

2.2. Catalytic reactivity and kinetics evaluation

The catalytic reactivity of the B-site-substituted $CaMFeO_3$ catalysts was evaluated in oxidative degradation of AOII (35 mg L^{-1}) by dispersing 0.1 g catalyst in 100 mL of AOII solution and 22 mM of H_2O_2 at room temperature stirred at 200 rpm for 90 min. At regular interval, 5 mL of reaction suspension was withdrawn and filtered through a 0.2 μm filter syringe. UV–vis spectrophotometer (Perkin Elmer, Lambda 25) was used to determine the concentration of AOII solution at λ_{max} of 486 nm. Further, 2-propanol (Merck, 10 M) mixed in an AOII solution was used as hydroxyl radical ($^{\bullet}OH$) scavenger. The results are reproducible with duplicate experiments conducted. The data show average value with experimental errors of less than 5%. Details analysis on the identification of AOII's intermediate compounds are provided in Supplementary Information (Text S2).

3. Results and discussion

3.1. Catalyst characterization

Fig. 1 displays the XRD patterns of resultant $CaFeO_3$ and B-site-substituted $CaMFeO_3$ samples. The XRD pattern of $CaFeO_3$ sample exhibited four major peaks at 2θ of 33.56°, 35.48°, 37.82° and 49.84° corresponding to perovskite $CaFeO_3$ (COD 96–152–6749), whilst peaks at 2θ of 32.74° and 33.26° are related to perovskite-like structure (COD 96–152–0830) [40]. Impurity phases consist of calcium ferrite $CaFe_5O_7$ (COD 96–901–3961) is observed at 2θ of 34.04°, 34.78°, 36.16° and 40.16°, maghemite γ-Fe_2O_3 (COD 96–901–2692) at 2θ of 32.22° and 44.72°; and calcium oxide (COD 96–900–6746) at 2θ of 30.88°, 35.72° and 51.36°.

When Cu was partially substituted into the B-site of $CaFeO_3$, additional new peaks are observed at 2θ of 17.20°, 34.80° and 42.80° which corresponds well to perovskite $CaCu_{2.79}Fe_{4.21}O_{12}$ (COD 96–434–4870). Meanwhile, peaks at 2θ of 35.50° and 38.70° are assigned to copper oxide phase (COD 96–721–2242). Partial substitution of Co into the

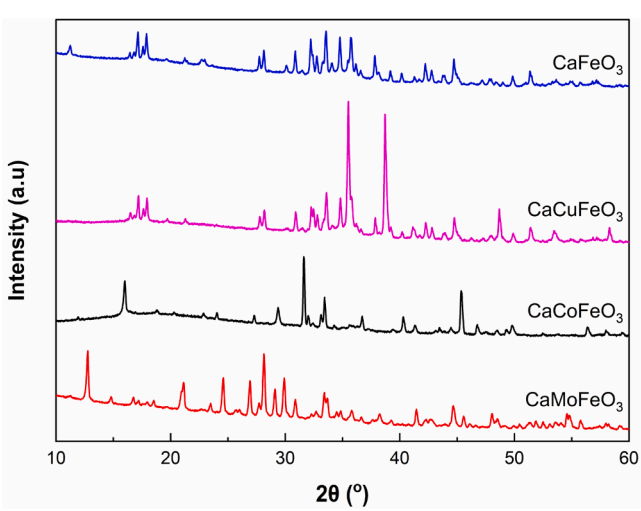

Fig. 1. XRD patterns of B-site substituted perovskite catalysts.

$CaFeO_3$ resulted in peaks at 2θ of 33.44° that are ascribed to perovskite Ca_2FeCoO_5 (COD 96–400–0920). Cobalt (II) oxide (COD 96–153–1762) is also noticeable at 2θ of 16.00°. In the case of partial substitution of Mo, perovskite phases appeared at 2θ of 32.68° that corresponds to Ca_2FeMoO_6 (COD 96–400–2219). Peaks at 2θ of 24.60°, 27.72°, 29.92° and 34.84° are assigned to $Fe_2(MoO_4)_3$ (COD 96–152–4203). Moreover, the peaks at 2θ of 21.02°, 28.16° and 44.66° are attributed to orthorhombic $Mo_{15.39}O_{47}$ phase (COD 96–154–0782); whilst peaks at 2θ of 29.10° and 54.58° are related to $CaMoO_4$ (COD 96–900–9634). Hence, these findings confirm that the resultant $CaFeO_3$ and B-site-substituted $CaMFeO_3$ samples contained mixtures of perovskites and mixed oxides phases.

The surface morphology of the samples was analyzed by FE-SEM as depicted in Fig. 2. All substituted perovskite catalysts exhibited heterogeneous surfaces which consists of irregular shape and sizes. $CaFeO_3$ mixed oxides shows the formation of rugged features consisting of larger particles and smaller particles showing lamellar structures that agglomerated during sintering. Changes in particle size can be clearly observed when transition metals of Cu, Mo and Co were partially substituted as demonstrated by the inset histograms. For instance, evolution of particle size can be observed in the sequence of $CaCuFeO_3$ < $CaFeO_3$ < $CaMoFeO_3$ < $CaCoFeO_3$. $CaCuFeO_3$ resulted in a narrow particle size distribution of small irregular particles (1–2 μm) and the most homogeneous sample. Contrary to this, the other mixed oxides consisted of a broader size distribution ranging from connected smaller particles (< 1 μm) forming rugged particles to larger particles (2–7 μm). This is clearly observed in $CaFeO_3$ < $CaMoFeO_3$ < $CaCoFeO_3$ samples, giving an indication that different phases were formed as evidenced in the XRD patterns (Fig. 1).

The elemental mapping (Fig. 3a-o) reveals that Ca, Fe, Mo, Cu, Co and O elements were evenly distributed throughout the surface of the catalysts. Further analysis indicates that the distribution of Cu and Co occurred as discrete particles at the surface of the catalysts whilst Mo distribution was relatively uniform. Table 1 presents the detailed composition of all catalysts. The composition of substituted Cu, Mo and Co into the perovskite and metal oxide structures were found to be 12.3, 12.2 and 14.5 wt%, respectively. The composition of Fe decreased from 31.6 wt% from the blank catalyst ($CaFeO_3$) to an average value of 25 wt % for the B-site-substituted $CaMFeO_3$. These results indicate the successful partial substitution of transition metals (Mo, Cu and Co) into the $CaFeO_3$ catalyst structures.

Fig. 4 illustrates the representative sorption isotherm of the resultant catalysts. All catalysts produced low N_2 sorption volumes, a clear indication of the formation of non-porous materials. Although the isotherms are of type III with a hysteresis loop at $p/p_0 > 0.45$, this is not associated with mesopores but attributed to the spacing within the rugged small particles. This is clearly seen in the SEM images for $CaFeO_3$, $CaMoFeO_3$ and $CaCoFeO_3$ samples. The $CaCuFeO_3$ sample consisted mainly of smaller particle with a narrow distribution (Fig. 2) and the hysteresis is ascribed to the smaller interparticle spacing. For the increase in the sorption volume at $p/p_0 > 0.9$, this is generally related to the larger interparticle spacing. The blank sample $CaFeO_3$ resulted in the highest surface area, attributed to the rugged surfaced in the FE-SEM image (Fig. 2). The BET surface areas were 12.8 m^2 g^{-1} ($CaFeO_3$), 6.0 m^2 g^{-1} ($CaCuFeO_3$), 3.5 m^2 g^{-1} ($CaCoFeO_3$) and 2.0 m^2 g^{-1} ($CaMoFeO_3$).

The profiles of O_2-TPD analysis are shown in Fig. 5a. It can be observed that all catalysts exhibit dominant peaks between 561°C to 590°C. The O_2 uptake decreased from 1.02 mmol g^{-1} ($CaFeO_3$) to 0.50 mmol g^{-1} ($CaCuFeO_3$), 0.42 mmol g^{-1} ($CaMoFeO_3$) and 0.18 mmol g^{-1} ($CaCoFeO_3$). Therefore, partially substituting the B-site with metals (Cu, Co and Mo) reduced the overall O_2 uptake. Further, these results confirm that all catalysts tested in this work have oxygen related sites with potential active sites for H_2O_2 activation during catalysis. The H_2-TPR profile of all catalysts in Fig. 5b exhibits well-defined reduction peak at a temperature range between 638 and 651°C. This temperature range corresponds to the partial reduction of Fe^{3+} to Fe^{2+} [41]. Interestingly,

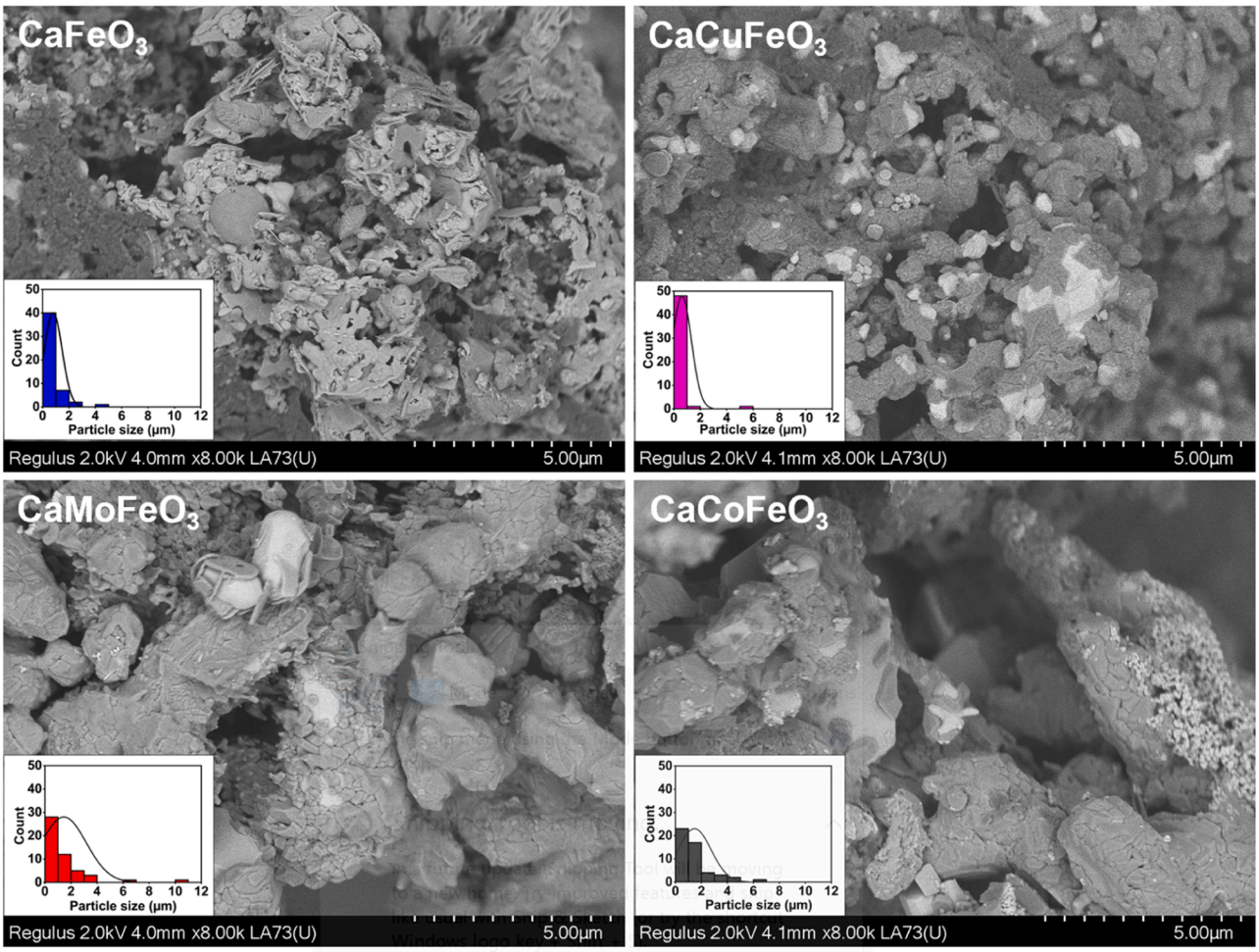

Fig. 2. FE-SEM images and corresponding inset histogram of particle size distributions of the B-site substituted perovskite catalysts.

two reduction peaks observed at 225 and 271°C was observed for the $CaCuFeO_3$. These peaks can be attributed to the reduction of Cu^{2+} to Cu^{+} and Cu^{+} to Cu [42]. The hydrogen consumption of $CaCuFeO_3$ started at a much lower temperature compared to other catalysts, suggesting the high-valence-state copper/iron ions in $CaCuFeO_3$ are more easily reduced to a lower oxidation state than those in $CaFeO_3$, $CaCoFeO_3$ and $CaMoFeO_3$ in this work. In other words, copper/iron ions in $CaCuFeO_3$ are better electron acceptors, which can efficiently accelerate the redox cycle during catalysis.

3.2. Catalytic performance

The performance of the catalysts for AOII oxidation in the absence and presence of H_2O_2 are presented in Fig. 6. In the absence of H_2O_2, the adsorption capacities $CaFeO_3$, $CaCuFeO_3$, $CaMoFeO_3$ and $CaCoFeO_3$ for AOII removal were 25%, 28%, 14% and 12% within 60 min, respectively. The low AOII adsorption is due to strong repulsion between the negative-charged of perovskite catalyst (Fig. S1) and anionic AOII behavior. Heterogeneous Fenton-like degradation of AOII in the presence of H_2O_2 was used as a model reaction to evaluate the catalytic reactivity of the catalysts quantitatively. Fig. 6 shows that no AOII removal was observed in the presence of H_2O_2 alone. In the presence of the catalysts and H_2O_2, the AOII removal was enhanced significantly. The overall catalytic performance improvement within 60 min of reaction were as follows: $CaCuFeO_3$ (97%) > $CaMoFeO_3$ (90%) > $CaFeO_3$ (64%) > $CaCoFeO_3$ (40%). This result reveals that mixed metal oxides and B-site substituted perovskite catalysts activated H_2O_2 to accelerate the generation of $^{\bullet}OH$ radicals, resulting in a much higher rate of AOII removal. The decomposition of AOII occurs mainly at the solid-liquid interfaces of the catalysts; where the activation of H_2O_2 took place.

It is interesting to observe that the $CaFeO_3$ had the highest surface area of 12.8 $m^2\ g^{-1}$ and highest O_2 uptake of 1.02 mmol g^{-1}, parameters of which significantly contribute to reaction performance. Contrary to this, AOII degradation by $CaFeO_3$ was relatively lower at 64%. This lack of performance is attributed to the lower reactivity of $CaFeO_3$ mixed oxides. Further, these results suggest that the smaller particles in the rugged surface as observed in the SEM image of $CaFeO_3$ (Fig. 2) which contribute to high surface area are related to a low performance of the $CaFeO_3$ mixed oxides phase. The $CaCuFeO_3$ catalyst resulted in the highest reaction performance of 97% though with a surface area and O_2 uptake around 50% that of the $CaFeO_3$ catalyst. In principle, the SEM image shows that $CaCuFeO_3$ catalyst constituted mainly of small particles with a narrow distribution and in overall terms more homogenous than the other catalysts tested in this work. Further, the high catalytic performance of $CaCuFeO_3$ was aided by the decent copper/iron redox coupling to activate H_2O_2 into $^{\bullet}OH$ radicals during catalysis.

The UV–vis spectra in Fig. 7a shows the evolution of AOII degradation by $CaCuFeO_3$ in the presence of H_2O_2. Several absorption peaks are present in the AOII solution prior to reaction at $t = 0$ min. For instance, two main peaks at 430 and 486 nm are attributed to the transition of the azo and hydrazone forms [43], while the other two peaks at 230 and 310 nm are assigned to the benzene and naphthalene rings [44] of AOII molecules. Noticeably, all peaks decreased as reaction time increased except for the peak at 254 nm. These results clearly indicate the destruction of azo bonds (at λ = 430 and 486 nm) and the opening of benzene and naphthalene rings (at λ = 230 and 310 nm) [29]. The

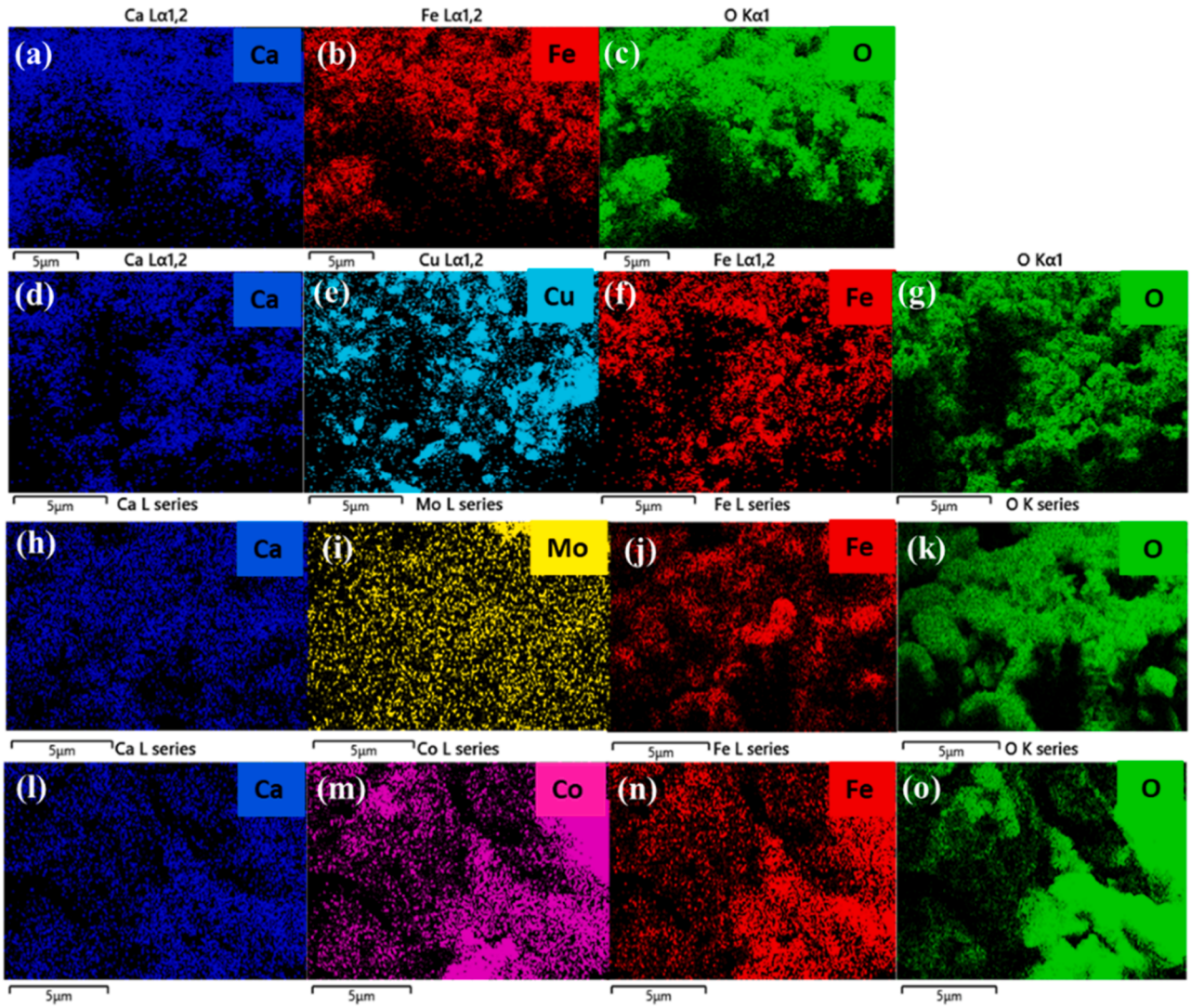

Fig. 3. Elemental mapping of (a-c) $CaFeO_3$, (d-g) $CaCuFeO_3$, (h-k) $CaMoFeO_3$ and (l-o) $CaCoFeO_3$ catalysts.

Table 1
Chemical composition of $CaFeO_3$, $CaCuFeO_3$, $CaMoFeO_3$ and $CaCoFeO_3$ by EDS analysis.

Samples	Chemical compositions (%)					
	Ca	Fe	O	Cu	Mo	Co
$CaCuFeO_3$	18.05	26.88	42.77	12.30	–	–
$CaMoFeO_3$	16.14	20.96	50.67	–	12.23	–
$CaCoFeO_3$	18.41	27.95	39.15	–	–	14.49
$CaFeO_3$	23.88	31.63	44.49	–	–	–

UV–vis spectra profiling of AOII by $CaFeO_3$, $CaMoFeO_3$ and $CaCoFeO_3$ catalysts (Fig. S2) indicate a lower efficiency of AOII degradation by these catalysts compared to $CaCuFeO_3$.

Further analysis on the intermediate peak profiling at $\lambda = 310$ nm and 254 nm are displayed in Figs. 7b and 7c for all catalysts. The peak intensity at 310 nm decreased significantly for the $CaCuFeO_3$ within 30 min with $C_t/C_o = 0.2$, followed by $CaFeO_3$ ($C_t/C_o = 0.6$), $CaCoFeO_3$ ($C_t/C_o = 0.7$) and $CaMoFeO_3$ ($C_t/C_o = 1.0$). These results indicate higher decomposition of naphthalene rings in the presence of $CaCuFeO_3$ compared to other catalysts. Nevertheless, the C_t/C_o intensity at $\lambda = 254$ nm increased over time due to the formation of benzene intermediate. From Fig. 7c, the C_t/C_o intensity doubled for $CaMoFeO_3$ and started to be levelled off after 30 min. Similar trend was observed for $CaFeO_3$, $CaCuFeO_3$ and $CaCoFeO_3$, which implied that the benzene intermediates were not degraded during this period. The presence of intermediate compounds was identified by GCMS analysis. Detailed chromatogram and proposed chemical structure of the intermediates (1,3-benzenediol, 2-acethyl; 2,6-dihydroxybenzoic acid; 3-hydroxy-benzoic acid; 2-heptanol,6-amino-2-methyl; 3-hydroxy-3-methyl-benzoic acid; 4-(1,2-dihydroxyethyl)−1,2-benzenediol) were summarized in Fig. S3 and Table S1, respectively. Hence, the oxidative degradation mechanism of AOII is proposed as presented in Fig. 8.

The oxidative degradation of AOII by all catalysts fits a pseudo-second-order reaction kinetics model ($R^2 > 0.93$) as shown in Fig. 9a following Eq. (1) and its integrated form Eq. (2):

$$\frac{dC_t}{dt} = -k(C_t)^2 \tag{1}$$

$$\frac{1}{C_t} = \frac{1}{C_0} + kt \tag{2}$$

where k (L mg^{-1} min^{-1}) is an apparent kinetics rate constant of second-order, t is reaction time, and C_t is AOII concentration at a given time t. The reaction rate constants are given in Fig. 9b. It is observed that $CaCuFeO_3$ ($k = 1.9 \times 10^{-2}$ L mg^{-1} min^{-1}) was the highest value followed by $CaMoFeO_3$ ($k = 4.5 \times 10^{-3}$ L mg^{-1} min^{-1}). These reaction rate constants were higher by factors of twenty-one and five times than that

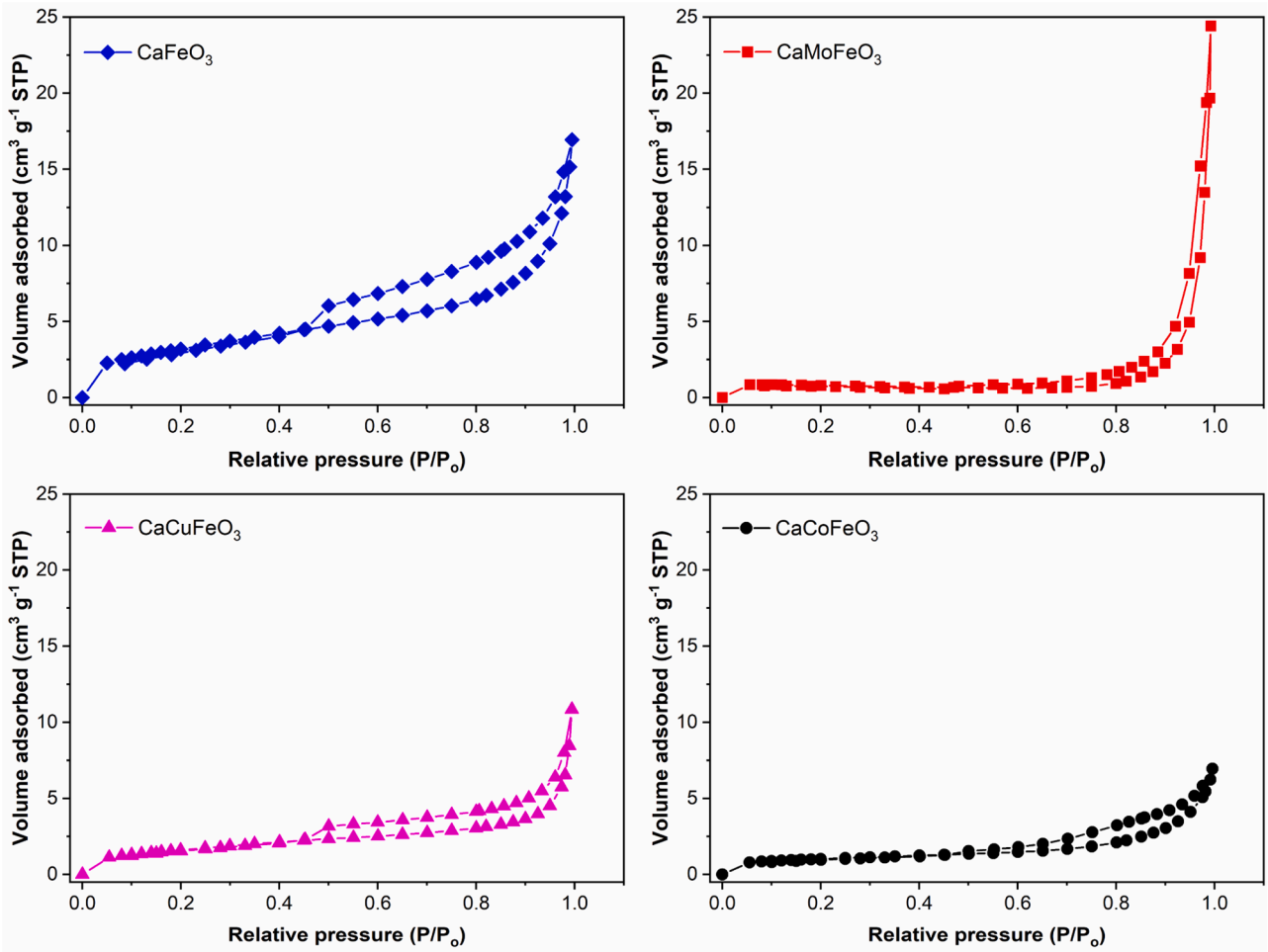

Fig. 4. Nitrogen adsorption/desorption isotherms of the catalysts.

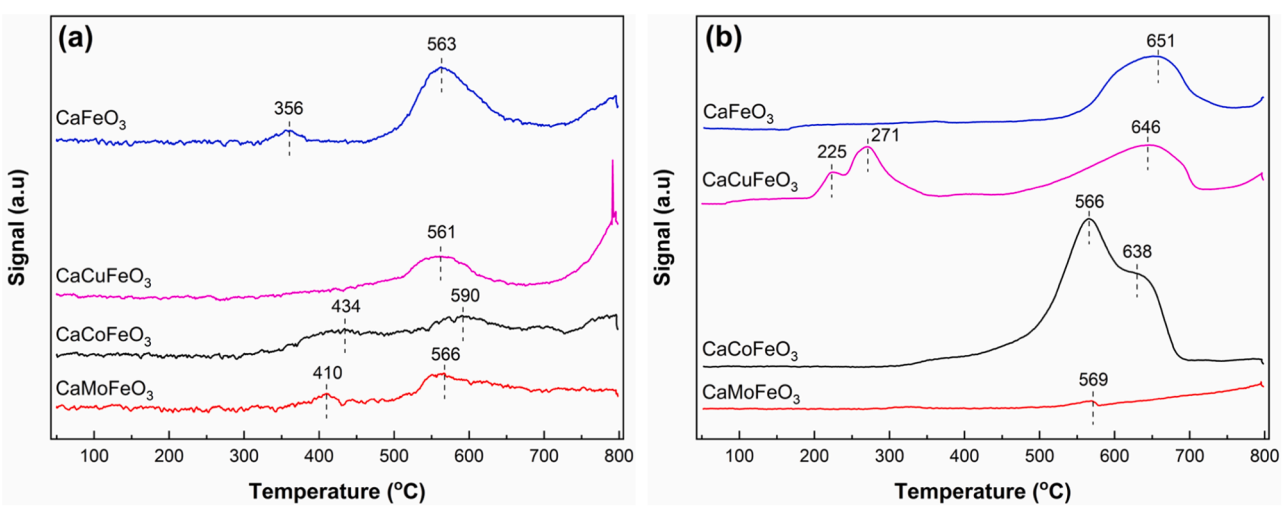

Fig. 5. (a) O_2-TPD and (b) H_2-TPR of the catalysts.

of $CaFeO_3$ ($k = 0.9 \times 10^{-3}$ L mg^{-1} min^{-1}), respectively. $CaCoFeO_3$ yielded the lowest reaction rate constant of ($k = 0.3 \times 10^{-3}$ L mg^{-1} min^{-1}). The kinetic behavior of all the catalysts can be well supported by the magnitude of electron transfer rate. Interestingly, $CaCuFeO_3$ exhibited the lowest electron transfer resistance as indicated by the smallest arc diameter compared to others $CaMFeO_3$ (M = Mo, Co) which are presented in Fig. 9c. The low resistance implies a faster electron transfer mobility and a higher surface reaction rate [45–47]. Faster electron transfer is beneficial to facilitate fast redox cycling of active sites during catalysis. The evolution of electron transfer rate and surface reaction rate can be observed in the order of $CaCuFeO_3 > CaMoFeO_3 > CaFeO_3 > CaCoFeO_3$. For comparison purposes, Fig. 9d displays the performance of $CaCuFeO_3$ against various catalysts containing La, Ca and CaSr in the A-site, and Co, Cu, Fe, Ni, NiFe and NiCu in the B-site.

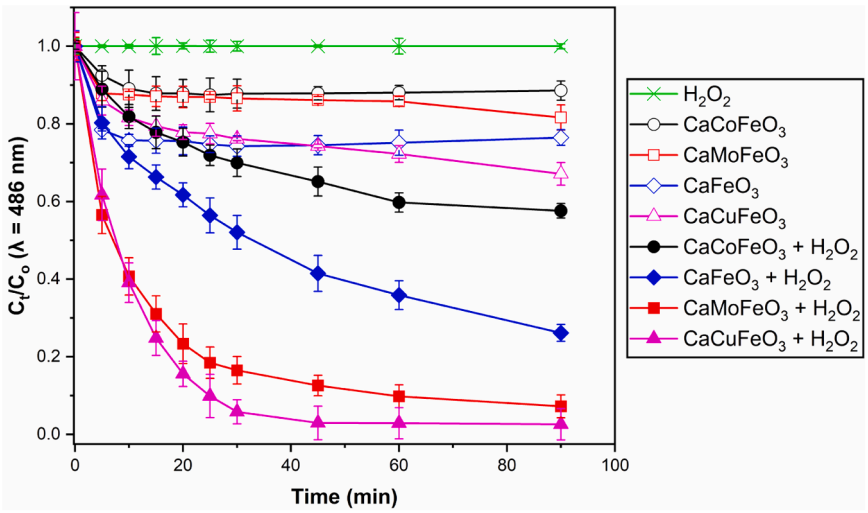

Fig. 6. Removal profile of AOII solution by $CaFeO_3$, $CaCuFeO_3$, $CaMoFeO_3$ and $CaCoFeO_3$ in the absence and presence of H_2O_2. Experimental conditions: AOII 35 mg L^{-1}, H_2O_2 22 mM, 1.0 g L^{-1} catalyst and unadjusted pH solution.

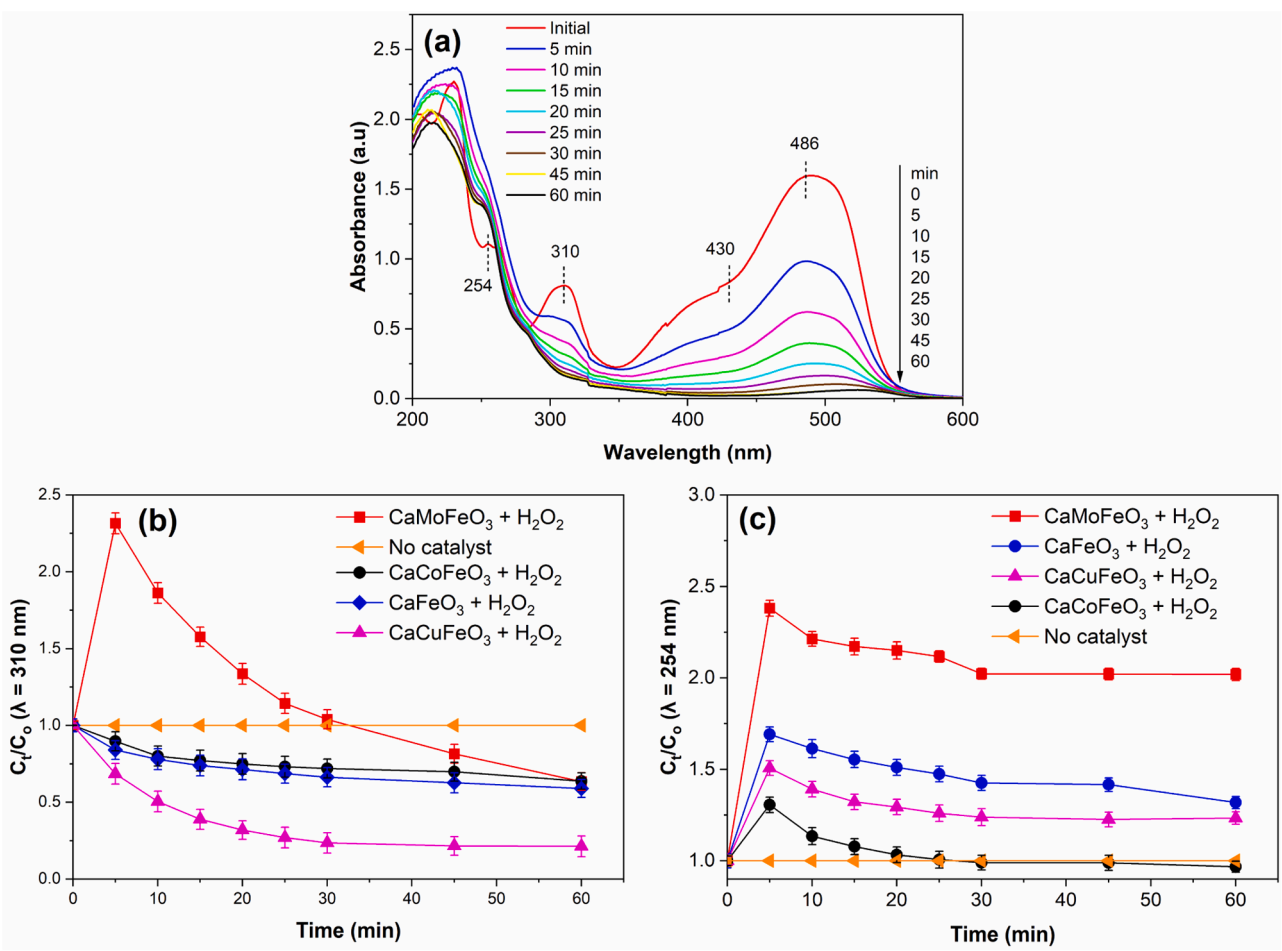

Fig. 7. UV–vis spectra of AOII degradation as a function of time by (a) $CaCuFeO_3$ and the normalized peak intensity at (b) 310 nm and (c) 254 nm by $CaFeO_3$, $CaCuFeO_3$, $CaMoFeO_3$ and $CaCoFeO_3$ in the presence of H_2O_2. Experimental conditions: AOII 35 mg L^{-1}, H_2O_2 22 mM, 1.0 g L^{-1} catalyst and unadjusted pH solution.

$CaCuFeO_3$ outperformed all catalysts for the degradation of AOII and other dyes, with the exception of $LaCoO_3$. Further additional comparison on others relevant aspects is also provided in Table S2.

The influence of key operational reaction conditions (catalyst dosage, initial pH solution, initial H_2O_2 concentration, initial AOII concentration and temperature) on the AOII degradation in the presence of $CaCuFeO_3$ catalyst is presented in Fig. S4. AOII degradation significantly enhanced from 16% to 99% as the catalyst dosage increased from 0.25 to 1.25 g/L within 60 min reaction time (Fig. S4a). The higher catalyst dosage led to the increased amount of active sites which are

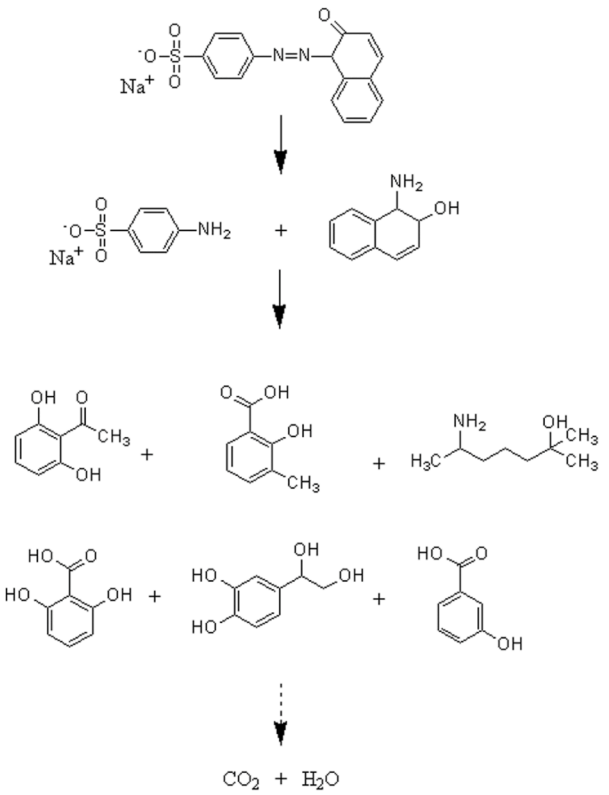

Fig. 8. Proposed AOII's oxidative degradation pathways in the presence of $CaCuFeO_3$ perovskite catalyst during heterogeneous Fenton-like catalysis.

responsible for the activation of H_2O_2 into $^{\bullet}OH$ radicals and thus enhancing the degradation of AOII [10]. Optimum dosage was found to be at 1.25 g/L as AOII degradation reached a plateau beyond this value.

Fig. S4b reveals that the AOII degradation (≈ 99%) was favorable within broad range of pH 3 to 8. However, the AOII degradation efficiency decreased to 88% when pH reduced to 2.5, which can be ascribed to the scavenging effect of $^{\bullet}OH$ radicals by the excessive amount of H^+ [49]. Hence, the unadjusted pH (pH 6.4) is selected as optimum pH solution due to its high AOII degradation of 99% without the need of pH adjustment. Interestingly, the AOII degradation was not significantly influenced by the H_2O_2 concentration. The AOII degradation reached 99% for all H_2O_2 concentration ranging from 11 to 44 mM within 60 min of reaction (Fig. S4c). From the degradation profiling, 22 mM of H_2O_2 concentration was chosen as the optimum oxidant concentration because it resulted in the highest AOII removal within the shortest reaction time (92% degradation in 20 min). The influence of AOII concentration is presented in Fig. S4d. The AOII degradation reached 99% as the AOII concentration increases from 25 to 55 mg/L within 60 min of reaction. However, the AOII degradation profiling at low AOII concentration (25 to 35 mg/L) was favorable instead of high concentration (45 to 55 mg/L). Hence, 35 mg/L of AOII concentration was chosen as the optimum value as it represents the nominal dye concentration in previously reported works [10,28]. Enhanced AOII degradation was observed at 50°C which reached 99% in less than 15 min (Fig. S4e). The contact between H_2O_2 and active sites may increase when the solution's temperature increases, thus promoting the generation of $^{\bullet}OH$ radicals [29,50].

The reusability of the $CaCuFeO_3$ perovskite catalyst for AOII degradation was performed in five consecutive cycles of reaction (Fig. S5). The degradation efficiency of AOII remained unchanged (>90%) in the first three cycles. However, AOII degradation efficiency started to decrease at the fourth cycle that could be attributed to partial saturation of intermediates on the active sites and thus hindering the effective formation of $^{\bullet}OH$ radicals as reported elsewhere [51,52]. Interestingly, low metal leaching (Cu <0.25 mg/L and Fe <0.04 mg/L) was observed. These values are significantly lower than the allowable limit of 1.0 mg/L (Cu) and 5.0 mg/L (Fe) under Malaysian Regulatory Act discharge criteria [53] and previously reported works [28,54,55].

In order to further understand the high performance of the $CaCuFeO_3$ catalyst, a possible mechanism for the degradation of AOII is proposed as schematically shown in Fig. 10 and Eqs. (3) to (10). Based on the O_2-TPD results, the partially substituted Cu at the B-site of $CaFeO_3$ has led to the formation of oxygen vacancies to maintain charge neutrality Eq. (3)). $V_0^{\bullet\bullet}$ stands for oxygen vacancy which are present on the surface of $CaCuFeO_3$, whilst O_0^x represents the divalent O ion. These oxygen vacancies could result in a lower Fe and Cu oxidation state (Eqs. (4) and ((5)), leading to more efficient Fe/Cu redox cycles. For instance, the reduction of $\equiv Fe^{3+}$ to $\equiv Fe^{2+}$ by $\equiv Cu^{+}$ is thermodynamically beneficial because the standard reduction potential of Fe^{3+}/Fe^{2+} (0.77 V) is higher than that of Cu^{2+}/Cu^{+} (0.34 V) Eq. (6)). Besides, the regeneration of active sites ($\equiv Fe^{2+}$ and $\equiv Cu^{+}$) catalytically activated the adsorbed H_2O_2 into $^{\bullet}OH$ radicals (Eqs. (7) and ((8)). The formation of $^{\bullet}OH$ radicals was further enhanced by H_2O_2 activation (Eq. (9)), which is attributed to the cleavage of O—O bond due to oxygen vacancies in perovskites [47,56] such as $CaCuFeO_3$ in this work. The generation of $^{\bullet}OH$ radicals were confirmed by adding 2-propanol as $^{\bullet}OH$ quenchers into the reaction mixture during catalysis. In the presence of 2-propanol, the overall catalytic performance decreased from 97% to 65% as illustrated in the Fig. S6. Hence, this result confirms that the generation of $^{\bullet}OH$ radicals is responsible for AOII degradation (Eq. (10)) in line with works reported elsewhere [36,57].

$$\equiv Fe^{3+} + \equiv Cu^{2+} + O_o^x \rightarrow \equiv FeCu + V_o^{\bullet\bullet} \tag{3}$$

$$V_o^{\bullet\bullet} + \equiv Fe^{3+} \rightarrow \equiv Fe^{2+} + O_o^x \tag{4}$$

$$V_o^{\bullet\bullet} + \equiv Cu^{2+} \rightarrow \equiv Cu^{+} + O_o^x \tag{5}$$

$$\equiv Fe^{3+} + Cu^{+} \rightarrow \equiv Fe^{2+} + Cu^{2+} \ (E^o = 0.43V) \tag{6}$$

$$\equiv Fe^{2+} + H_2O_2 \rightarrow \equiv Fe^{3+} + OH^- + {}^{\bullet}OH \tag{7}$$

$$\equiv Cu^{+} + H_2O_2 \rightarrow \equiv Cu^{2+} + OH^- + {}^{\bullet}OH \tag{8}$$

$$V_o^{\bullet\bullet} + H_2O_2 \rightarrow 2\,{}^{\bullet}OH \tag{9}$$

$$AOII + {}^{\bullet}OH \rightarrow intermediate \rightarrow CO_2 + H_2O \tag{10}$$

4. Conclusion

A series of mixed oxide catalysts ($CaMoFeO_3$, $CaCuFeO_3$ and $CaCoFeO_3$) were successfully synthesized via the combined EDTA-citric acid complexation, containing both mixed oxides and B-partially substituted perovskite phases. The AOII oxidative degradation in the presence of H_2O_2 fitted a pseudo-second-order kinetics model. The order of reaction rate constant was found to be in the sequence of $CaCuFeO_3$ ($k = 1.9 \times 10^{-2}$ L mg^{-1} min^{-1}) > $CaMoFeO_3$ ($k = 4.5 \times 10^{-3}$ L mg^{-1} min^{-1}) > $CaFeO_3$ ($k = 0.9 \times 10^{-3}$ L mg^{-1} min^{-1}) > $CaCoFeO_3$ ($k = 0.3 \times 10^{-3}$ L mg^{-1} min^{-1}). The enhanced catalytic reactivity of $CaCuFeO_3$ was attributed to the fast redox cycling of active sites due to the high reducibility of copper/iron ions and the decent electron mobility within the structure of the catalyst that facilitates efficient generation of reactive radicals during catalysis. In fact, the $CaCuFeO_3$ catalyst has also shown decent catalytic performance over five cycles of reactions with significantly low metal leaching that are well below the permissible discharge limit.

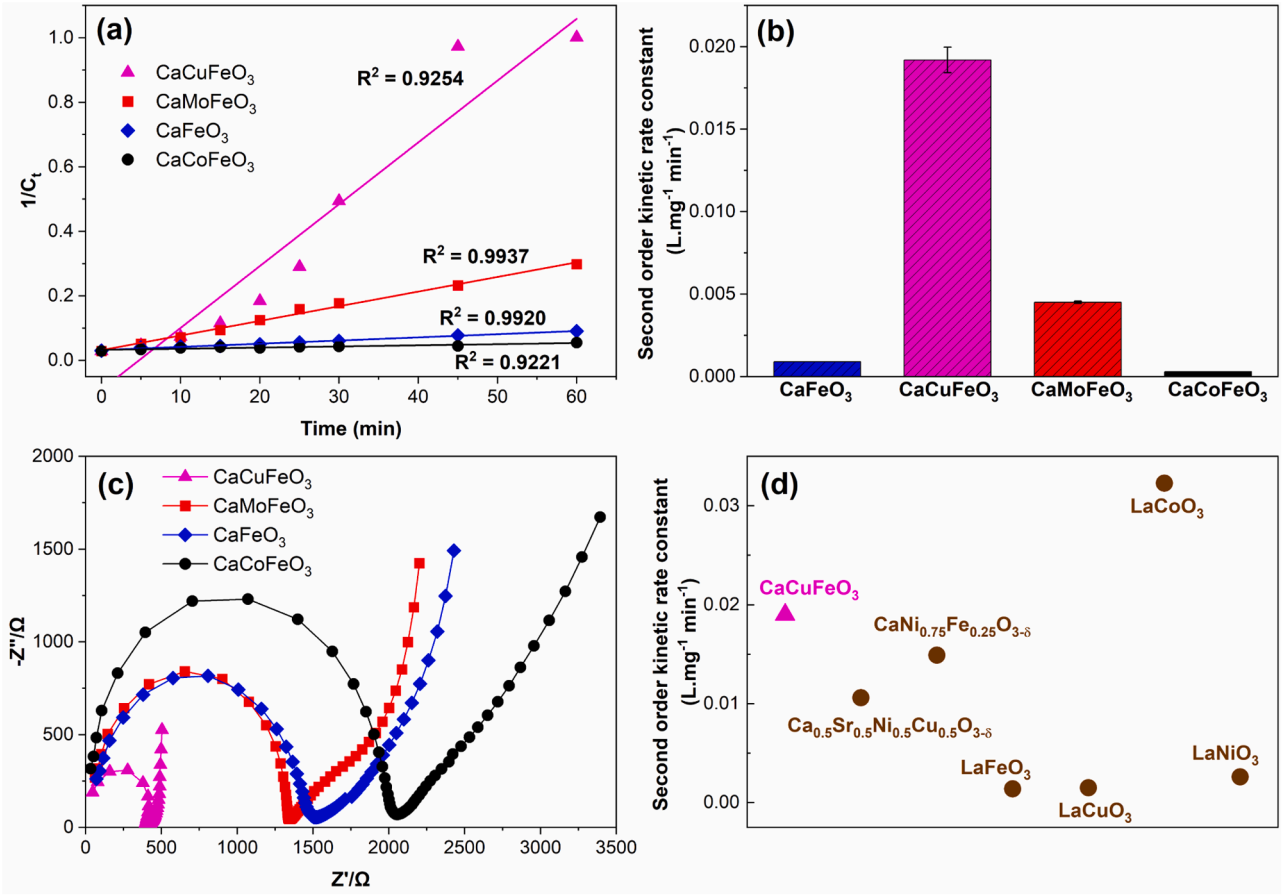

Fig. 9. (a) AOII removal in the presence of H_2O_2 using second-order reaction kinetics models, (b) rate constant of the perovskite catalysts, (c) Nyquist plot of the perovskite catalysts and (d) comparison of rate constant between $CaCuFeO_3$ (this work) and others reported B-site perovskite catalysts particularly to dye-contaminated remediation ($LaFeO_3$, $LaCuO_3$, $LaNiO_3$ and $LaCoO_3$ [48]; $Ca_{0.5}Sr_{0.5}Ni_{0.5}Cu_{0.5}O_{3-\delta}$ [28]; $CaNi_{0.75}Fe_{0.25}O_{3-\delta}$ [29]). Experimental conditions: AOII 35 mg L^{-1}, H_2O_2 22 mM, 1.0 g L^{-1} catalyst and unadjusted pH solution.

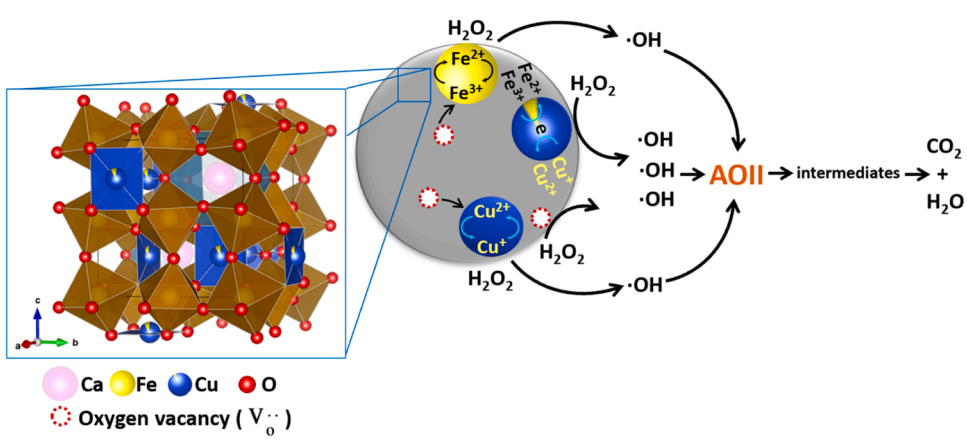

Fig. 10. Possible mechanism for AOII degradation by $CaCuFeO_3$.

Declaration of Competing Interest

The authors declare that they have no known competing financial interests or personal relationships that could have appeared to influence the work reported in this paper.

Acknowledgments

The authors would like to acknowledge the Ministry of Higher Education Malaysia (MOHE) and Universiti Teknologi MARA Cawangan Pulau Pinang for the financial support under Fundamental Research Grant Scheme (600-IRMI/FRGS 5/3 (158/2019)) and the Sydney Southeast Asia Centre for the Collaborative Research Grant (100-TNCPI/INT 16/6/2 (006/2022)). The authors also acknowledge the scientific and technical assistance of the EMZI-UiTM Nanoparticles Colloids & Interface Industrial Research Laboratory (NANO—CORE), Universiti Teknologi MARA. R. Alrozi gratefully acknowledges the generous financial support from Ministry of Higher Education Malaysia (MOHE)

and Universiti Teknologi MARA (UiTM) for her study leave. J. C. Diniz da Costa gratefully thank as invited Professor funded by the Associate Laboratory for Green Chemistry – LAQV, financed by the National Portuguese funds from FCT/MCTES (UIDB/50006/2020).

Supplementary materials

Supplementary material associated with this article can be found, in the online version, at doi:10.1016/j.jtice.2023.104675.

References

[1] Ali H. Biodegradation of synthetic dyes - A review. Water Air Soil Pollut 2010;213:251–73.
[2] Martínez-Huitle CA, Brillas E. Decontamination of wastewaters containing synthetic organic dyes by electrochemical methods: a general review. Appl Catal B Environ 2009;87:105–45.
[3] Christie R. Environmental aspects of textile dyeing. 1st ed. Cambridge, England: Woodhead; 2007.
[4] Duman O, Tunç S, Bozoğlan BK, Polat TG. Removal of triphenylmethane and reactive azo dyes from aqueous solution by magnetic carbon nanotube-κ-carrageenan-Fe_3O_4 nanocomposite. J Alloy. Compd 2016;687:370–83.
[5] Bustos-Terrones YA, Hermosillo-Nevárez JJ, Ramírez-Pereda B, Vaca M, Rangel-Peraza JG, Bustos-Terrones V, et al. Removal of BB9 textile dye by biological, physical, chemical, and electrochemical treatments. J Taiwan Inst Chem Eng 2021;121:29–37.
[6] Shabir M, Yasin M, Hussain M, Shafiq I, Akhter P, Nizami AS, et al. A review on recent advances in the treatment of dye-polluted wastewater. J Ind Eng Chem 2022;112:1–19.
[7] Bafana A, Devi SS, Chakrabarti T. Azo dyes: past, present and the future. Environ Rev 2011;19:350–70.
[8] Kagalkar AN, Jagtap UB, Jadhav JP, Bapat VA, Govindwar SP. Biotechnological strategies for phytoremediation of the sulfonated azo dye Direct Red 5B using Blumea malcolmii Hook. Bioresour Technol 2009;100:4104–10.
[9] Chen Y, Yan X, Lin H, Wang C, Xu J. Enhanced Fenton-like degradation of Rhodamine B and Congo red by benzene and K^+ co-doped carbon nitride with *in situ*-generated H_2O_2. J Taiwan Inst Chem Eng 2022;131:104179.
[10] Zubir NA, Yacou C, Zhang X, Diniz da Costa JC. Optimisation of graphene oxide – iron oxide nanocomposite in heterogeneous Fenton-like oxidation of Acid Orange 7. J Environ Chem Eng 2014;2:1881–8.
[11] Yang C, Wang X, Zhang L, Dong W, Yang C, Shi X, et al. Investigation of kinetics and mechanism for the degradation of antibiotic norfloxacin in wastewater by UV/H_2O_2. J Taiwan Inst Chem Eng 2020;115:117–27.
[12] Cobo-Golpe M, Fernández-Fernández V, Arias T, Ramil M, Cela R, Rodríguez I. Comparison of UV, chlorination, UV-hydrogen peroxide and UV-chlorine processes for tramadol removal: kinetics study and transformation products identification. J Environ Chem Eng 2022;10:107854.
[13] Kusic H, Koprivanac N, Srsan L. Azo dye degradation using Fenton type processes assisted by UV irradiation: a kinetic study. J Photochem Photobiol A Chem 2006;181:195–202.
[14] Yang S, Wang P, Yang X, Shan L, Zhang W, Saho X, et al. Degradation efficiencies of azo dye acid orange 7 by the interaction of heat, UV and anions with common oxidants: persulfate, peroxymonosulfate and hydrogen peroxide. J Hazard Mater 2010;179:552–8.
[15] Taran OP, Ayusheev AB, Ogorodnikova OL, Prosvirin IP, Isupova LA, Parmon VN. Perovskite-like catalysts $LaBO_3$ (B=Cu, Fe, Mn, Co, Ni) for wet peroxide oxidation of phenol. Appl Catal B Environ 2016;180:86–93.
[16] Tian FX, Ye WK, Xu B, Hu XJ, Ma SX, Lai F, et al. Comparison of UV-induced AOPs (UV/Cl_2, UV/NH_2Cl, UV/ClO_2 and UV/H_2O_2) in the degradation of iopamidol: kinetics, energy requirements and DBPs-related toxicity in sequential disinfection processes. Chem Eng J 2020;398:125570.
[17] Ngumba E, Gachanja A, Tuhkanen T. Removal of selected antibiotics and antiretroviral drugs during post-treatment of municipal wastewater with UV, UV/chlorine and UV/hydrogen peroxide. Water Environ J 2020;34:692–703.
[18] Konstantinou IK, Albanis TA. TiO_2-assisted photocatalytic degradation of azo dyes in aqueous solution: kinetic and mechanistic investigations a review. Appl Catal B Environ 2004;49:1–14.
[19] Zubir NA, Yacou C, Motuzas J, Zhang X, Diniz Da Costa JC. Structural and functional investigation of graphene oxide-Fe_3O_4 nanocomposites for the heterogeneous Fenton-like reaction. Sci Rep 2014;4:1–8.
[20] Zubir NA, Yacou C, Motuzas J, Zhang X, Zhao XS, Diniz Da Costa JC. The sacrificial role of graphene oxide in stabilising a Fenton-like catalyst GO-Fe_3O_4. Chem Commun 2015;51:9291–3.
[21] Zhang Y, Liu H, Gao F, Tan X, Cai Y, Hu B, et al. EnergyChem Application of MOFs and COFs for photocatalysis in CO_2 reduction, H_2 generation, and environmental treatment. EnergyChem 2022;4:100078.
[22] Liu X, Zhou Y, Zhang J, Tang L, Luo L, et al. Iron containing metal − organic frameworks : structure, synthesis, and applications in environmental remediation. ACS Appl Mater Interfaces 2017;24:20255–75.
[23] Chen H, Motuzas J, Martens W, Diniz da Costa JC. Improved dark ambient degradation of organic pollutants by cerium strontium cobalt perovskite. J Environ Sci 2020;90:110–8 (China).
[24] Wang D, Luo X, Yang S, Xue G. Tourmaline/Perovskite composite material as heterogeneous catalysts for activation peroxymonosulfate to remove organic dye in water. J Environ Chem Eng 2021;9:105221.
[25] Wang Y, Chen L, Cao H, Chi Z, Chen C, et al. Role of oxygen vacancies and Mn sites in hierarchical $Mn_2O_3/LaMnO_{3-\Delta}$ perovskite composites for aqueous organic pollutants decontamination. Appl Catal B Environ 2019;245:546–54.
[26] Peña MA, Fierro JLG. Chemical structures and performance of perovskite oxides. Chem Rev 2001;101:1981–2017.
[27] Lu S, Wang G, Chen S, Yu H, Ye F, et al. Heterogeneous activation of peroxymonosulfate by $LaCo_{1-x}Cu_xO_3$ perovskites for degradation of organic pollutants. J Hazard Mater 2018;353:401–9.
[28] Chen H, Motuzas J, Martens W, Diniz Da Costa JC. Effective degradation of azo dyes in the dark by Cu^{2+} active sites in CaSrNiCu oxides. J Environ Chem Eng 2018;6:5870–8.
[29] Besegatto SV, da Silva A, Campos CEM, de Souza SMAGU, de Souza AAU, et al. Perovskite-based Ca-Ni-Fe oxides for azo pollutants fast abatement through dark catalysis. Appl Catal B Environ 2021;284:119747.
[30] Phan TTN, Nikoloski AN, Bahri PA, Li D. Heterogeneous photo-Fenton degradation of organics using highly efficient Cu-doped $LaFeO_3$ under visible light. J Ind Eng Chem 2018;61:53–64.
[31] Wang G, Cheng C, Zhu J, Wang L, Gao S, et al. Enhanced degradation of atrazine by nanoscale $LaFe_{1-x}Cu_xO_{3-\delta}$ perovskite activated peroxymonosulfate: performance and mechanism. Sci Total Environ 2019;673:565–75.
[32] Mao J, Quan X, Wang J, Gao C, Chen S, et al. Enhanced heterogeneous Fenton-like activity by Cu-doped $BiFeO_3$ perovskite for degradation of organic pollutants. Front Environ Sci Eng 2018;12:2–11.
[33] Ben S, Zhao F, Safaei Z, Lakshamy D. Sulfate radical-mediated degradation and mineralization of bisphenol F in neutral medium by the novel magnetic Sr_2CoFeO_6 double perovskite oxide catalyzed peroxymonosulfate : influence of co-existing chemicals and UV irradiation. Appl Catal B Environ 2018;233:99–111.
[34] Liu F, Qiao J, Li C, Meng H, Huang X. The study on photocatalytic degradation of Methyl Orange using $SrFe_{0.5}Co_{0.5}O_{3-\delta}$. Appl Mech Mater 2014;576:45–8.
[35] Duan X, Su C, Miao J, Zhong Y, Shao Z, et al. Insights into perovskite-catalyzed peroxymonosulfate activation: maneuverable cobalt sites for promoted evolution of sulfate radicals. Appl Catal B Environ 2018;220:626–34.
[36] Chen H, Motuzas J, Martens W, Diniz da Costa JC. Degradation of azo dye Orange II under dark ambient conditions by calcium strontium copper perovskite. Appl Catal B Environ 2018;221:691–700.
[37] Chen H, Motuzas J, Martens W, Diniz da Costa JC. Ceramic metal oxides with Ni^{2+} active phase for the fast degradation of Orange II dye under dark ambiance. Ceram Int 2018;44:6634–40.
[38] Riaz N, Chong FK, Dutta BK, Man ZB, Khan MS, et al. Photodegradation of Orange II under visible light using Cu-Ni/TiO_2: effect of calcination temperature. Chem Eng J 2012;185–186:108–19.
[39] Collivignarelli MC, Abbà A, Carnevale Miino M, Damiani S. Treatments for color removal from wastewater: state of the art. J Environ Manag 2019;236:727–45.
[40] Asenath-Smith E, Lokuhewa IN, Misture ST, Edwards DD. p-Type thermoelectric properties of the oxygen-deficient perovskite $Ca_2Fe_2O_5$ in the brownmillerite structure. J Solid State Chem 2010;183:1670–7.
[41] Rao YF, Zhang Y, Han F, Guo H, Huang Y, et al. Heterogeneous activation of peroxymonosulfate by $LaFeO_3$ for diclofenac degradation: DFT-assisted mechanistic study and degradation pathways. Chem Eng J 2018;352:601–11.
[42] Fierro G, Lo Jacono M, Inversi M, Dragone R, Porta P. TPR and XPS study of cobalt – copper mixed oxide catalysts: evidence of a strong Co – Cu interaction. Top Catal 2000;10:39–48.
[43] Vannucci G, Cañamares MV, Prati S, Sanchez-Cortes S. Study of the azo-hydrazone tautomerism of Acid Orange 20 by spectroscopic techniques: UV–Visible, Raman, and surface-enhanced Raman scattering. J Raman Spectrosc 2020;51:1295–304.
[44] Ji P, Zhang J, Chen F, Anpo M. Study of adsorption and degradation of acid orange 7 on the surface of CeO_2 under visible light irradiation. Appl Catal B Environ 2009;85:148–54.
[45] Gao M, Sheng W, Zhuang Z, Fang Q, Gu S, et al. Efficient water oxidation using nanostructured α-nickel-hydroxide as an electrocatalyst. J Am Chem Soc 2014;136:7077–84.
[46] Gao P, Tian X, Fu W, Wang Y, Nie Y, et al. Copper in $LaMnO_3$ to promote peroxymonosulfate activation by regulating the reactive oxygen species in sulfamethoxazole degradation. J Hazard Mater 2021;411:125163.
[47] Su C, Duan X, Miao J, Zhong Y, Zhou W, et al. Mixed conducting perovskite materials as superior catalysts for fast aqueous-phase advanced oxidation: a mechanistic study. ACS Catal 2017;7:388–97.
[48] Lin KA, Chen Y, Lin Y. $LaMO_3$ perovskites (M = Co, Cu, Fe and Ni) as heterogeneous catalysts for activating peroxymonosulfate in water. Chem Eng Sci 2017;160:96–105.
[49] Navalon S, Dhakshinamoorthy A, Alvaro M, Garcia H. Heterogeneous Fenton catalysts based on activated carbon and related materials. ChemSusChem 2011;4:1712–30.
[50] Wu P, Luo X, Zhang S, Li K, Qi F. Novel near room-temperature and/or light driven Fe-doped $Sr_2Bi_2O_5$ photo/thermocatalyst for methylene blue degradation. Appl Catal A Gen 2015;497:216–24.
[51] Rusevova K, Kopinke F, Georgi A. Nano-sized magnetic iron oxides as catalysts for heterogeneous fenton-like reactions - influence of Fe (II)/Fe (III) ratio on catalytic performance. J Hazard Mater 2012;241–242:433–40.
[52] Xue X, Hanna K, Abdelmoula M, Deng N. Adsorption and oxidation of PCP on the surface of magnetite: kinetic experiments and spectroscopic investigations. Appl Catal B Environ 2009;89:432–40.

[53] Environmental Quality Act, Environmental quality industrial effluent regulations 2009 - _P.U.A_434-2009.pdf, Percetakan Nas. Malaysia Berhad. 2009.
[54] Cai C, Liu Y, Xu R, Zhou J, Zhang J, et al. Bicarbonate enhanced heterogeneous activation of peroxymonosulfate by copper ferrite nanoparticles for the efficient degradation of refractory organic contaminants in water. Chemosphere 2023;312:137285.
[55] Qin Q, Qiao N, Liu Y, Wu X. Spongelike porous CuO as an efficient peroxymonosulfate activator for degradation of Acid Orange 7. Appl Surf Sci 2020;521:146479.
[56] Wang H, Zhang L, Hu C, Wang X, Lyu L, et al. Enhanced degradation of organic pollutants over Cu-doped $LaAlO_3$ perovskite through heterogeneous Fenton-like reactions. Chem Eng J 2018;332:572–81.
[57] Tummino ML, Laurenti E, Deganello F, Bianco Prevot A, Magnacca G. Revisiting the catalytic activity of a doped $SrFeO_3$ for water pollutants removal: effect of light and temperature. Appl Catal B Environ 2017;207:174–81.